the situation in *M. lini*, where two paralogs of the *AvrL567* gene, exhibiting significant amino acid variation, show differential recognition and response by the *L5*, *L6*, and *L7* flax resistance genes (*9*). However, *ATR13* alleles, showing not only extensive amino acid variation but also deletions of repeated domains, were equally effective in triggering resistance via *RPP13-Nd*. The high level of amino acid variation among alleles that are recognized by RPP13-Nd may indicate that these variants are selectively favored in *H. parasitica* parasitizing host populations not expressing *RPP13-Nd*. To confirm that not all *H. parasitica* genes are undergoing an equivalent extreme rate of change, we sequenced *Ppat5* from the same *H. parasitica* isolates. *Ppat5* encodes a dnaK-type molecular chaperone (*16*) and hence is likely to be under different selective pressures as compared to *ATR13*. DNA sequence analysis of *Ppat5* revealed only nine segregating polymorphisms across the 1983–base pair ORF and, in contrast to ATR13, only one of these is a nonsynonymous polymorphism (*25*).

Our study reveals the *RPP13/ATR13* plant/pathogen interaction to be an excellent model for studying the coevolution of resistance and avirulence genes within host and pathogen populations. The high levels of amino acid polymorphism relative to silent polymorphism in both plant and pathogen genes is consistent with a history of balancing selection operating at both loci. Within RPP13, it is the LRR domain that shows diversifying selection, whereas the rest of the gene shows selection for conservation of protein sequence (*11*, *12*). This study shows that the C-terminal domain of ATR13 plays a role in determining the specificity of interaction with RPP13, suggesting a direct interaction with the LRR domain. However, our initial yeast two-hybrid studies have not revealed a direct interaction between RPP13 and ATR13 (*31*). It is possible that different alleles of RPP13 recognize other pathogen proteins, and variation at this locus could be influenced by additional pathogen interactions, not necessarily limited to *H. parasitica*. Additionally, ATR13 may be detected by more than one host resistance gene, leading to increased selection for diversity in this protein. ATR13 must have a role in enabling *H. parasitica* to grow as an obligate biotrophic pathogen on *Arabidopsis*, and the elucidation of the roles of the observed motifs in planta will add substantially to our understanding of the mechanisms of biotrophic pathogenicity as well as those of host defense.

References and Notes

1. J. L. Dangl, J. D. Jones, *Nature* **411**, 826 (2001).
2. D. A. Jones, J. D. Jones, *Adv. Bot. Res.* **24**, 90 (1997).
3. Y. Jia, S. A. McAdams, G. T. Bryan, H. P. Hershey, B. Valent, *EMBO J.* **19**, 4004 (2000).
4. L. Deslandes *et al.*, *Proc. Natl. Acad. Sci. U.S.A.* **100**, 8024 (2003).
5. M. H. Joosten, T. J. Cozijnsen, P. J. De Wit, *Nature* **367**, 384 (1994).
6. J. A. van Kan, G. F. van den Ackerveken, P. J. de Wit, *Mol. Plant Microbe Interact.* **4**, 52 (1991).
7. R. Luderer, F. L. Takken, P. J. de Wit, M. H. Joosten, *Mol. Microbiol.* **45**, 875 (2002).
8. M. J. Orbach, L. Farrall, J. A. Sweigard, F. G. Chumley, B. Valent, *Plant Cell* **12**, 2019 (2000).
9. P. N. Dodds, G. J. Lawrence, A.-M. Catanzariti, M. A. Ayliffe, J. G. Ellis, *Plant Cell* **16**, 755 (2004).
10. N. Westerink, R. Roth, H. A. Van den Burg, P. J. De Wit, M. H. Joosten, *Mol. Plant Microbe Interact.* **15**, 1219 (2002).
11. L. E. Rose *et al.*, *Genetics* **166**, 1517 (2004).
12. P. D. Bittner-Eddy, I. R. Crute, E. B. Holub, J. L. Beynon, *Plant J.* **21**, 177 (2000).
13. R. M. May, R. M. Anderson, in *Coevolution*, D. J. Futuyma, M. Slatkin, Eds. (Sinauer, Sunderland, MA, 1983), pp. 189–206.
14. J. B. S. Haldane, *Ricerca Sci.* **19** (suppl. 1), 68 (1949).
15. E. B. Holub, J. L. Beynon, I. R. Crute, *Mol. Plant Microbe Interact.* **7**, 223 (1994).
16. P. D. Bittner-Eddy, R. L. Allen, A. P. Rehmany, P. Birch, J. L. Beynon, *Mol. Plant Pathol.* **4**, 501 (2003).
17. Materials and methods are available as supporting material on *Science* Online.
18. N. T. Keen *et al.*, *Mol. Plant Microbe Interact.* **3**, 112 (1990).
19. Fusions of *Ppat17* were made with and without the predicted signal peptide sequence and were tested in the biolistic and in planta assays. Similar results were obtained with both forms of the gene.
20. R. L. Allen *et al.*, data not shown.
21. S. F. Altschul *et al.*, *Nucleic Acids Res.* **25**, 3389 (1997).
22. J. D. H. Bendtsen, Nielsen, G. von Heijne, S. Brunak, *J. Mol. Biol.* **340**, 783 (2004).
23. Q. Jin, R. Thilmony, J. Zwiesler-Vollick, S. Y. He, *Microbes Infect.* **5**, 301 (2003).
24. M. Hahn, K. Mendgen, *Curr. Opin. Plant Biol.* **4**, 322 (2001).
25. See supplementary figures on *Science* Online.
26. G. Van den Ackerveken, E. Marois, U. Bonas, *Cell* **87**, 1307 (1996).
27. GENECONV: A computer package for the statistical detection of gene conversion, S. A. Sawyer (1999). Distributed by the author, Department of Mathematics, Washington University, St. Louis, MO, and available at www.math.wustl.edu/~sawyer. The Geneconv method was used to determine whether some regions of a pair of sequences had more consecutive identical polymorphic sites than would be expected by chance. This test assumes that mutations are neutral and independently distributed and that there has been no history of recombination between sequences. Permutation of the sequences was used to assign *P* values to the observed shared fragments and to evaluate their statistical significance.
28. M. R. Grant *et al.*, *Science* **269**, 843 (1995).
29. E. A. Stahl, G. Dwyer, R. Mauricio, M. Kreitman, J. Bergelson, *Nature* **400**, 667 (1999).
30. J. Rozas, J. C. Sánchez-DelBarrio, X. Messeguer, R. Rozas, *Bioinformatics* **19**, 2496 (2003).
31. R. L. Allen, S. Hall, J. L. Beynon, unpublished results.

32. We thank H. Kaminaka and J. Dangl for allowing us to use pBDex; S. Bright, V. Buchanan-Wollaston, S. Hall, and B. Thomas for critical review of the manuscript; and E. Holub for provision of pathogen isolates. Supported by the Biotechnology and Biological Sciences Research Council and the Department of Environment, Food and Rural Affairs (under license PHL275/4864).

Supporting Online Material

www.sciencemag.org/cgi/content/full/306/5703/1957/DC1
Materials and Methods
Figs. S1 and S2
References

13 August 2004; accepted 22 October 2004
10.1126/science.1104022

Leading-Edge Vortex Lifts Swifts

J. J. Videler,[1,2]* E. J. Stamhuis,[1] G. D. E. Povel[2]

The current understanding of how birds fly must be revised, because birds use their hand-wings in an unconventional way to generate lift and drag. Physical models of a common swift wing in gliding posture with a 60° sweep of the sharp hand-wing leading edge were tested in a water tunnel. Interactions with the flow were measured quantitatively with digital particle image velocimetry at Reynolds numbers realistic for the gliding flight of a swift between 3750 and 37,500. The results show that gliding swifts can generate stable leading-edge vortices at small (5° to 10°) angles of attack. We suggest that the flow around the arm-wings of most birds can remain conventionally attached, whereas the swept-back hand-wings generate lift with leading-edge vortices.

The discovery of leading-edge vortices (LEVs) on the wings of insects in flight greatly advanced the knowledge of their dominant lift-generating mechanisms (*1, 2, 3*). Sharp leading edges induce high lift production through flow separation with vortical flow attached to the upper surface of insect wings during flapping and gliding.

[1]Department of Marine Biology (Experimental Marine Zoology Group), Groningen University, Post Office Box 14, 9750 AA, Haren, Netherlands. [2]Evolutionary Mechanics, Institute of Biology, Leiden University, Post Office Box 9516, 2300 RA Leiden, Netherlands.

*To whom correspondence should be addressed. E-mail: j.j.videler@biol.rug.nl

Avian wings, unlike insect and aircraft wings, consist of two distinct parts: an arm-wing and a hand-wing. Cross sections through arm-wings show conventional aerodynamic profiles with a rounded leading edge. In contrast, the leading edge of hand-wings is sharp, because it is the edge of the narrow vane of the outermost primary feather. Birds often use the hand-wings in a swept-back position forming a V-shaped wing configuration. Here, we apply digital particle image velocimetry (DPIV) (*4*, *5*) using models of the wing of the common swift (*Apus apus*), tested in a water tunnel, to investigate the lift generated by swept-back hand-wings of gliding birds (Fig. 1).

The common swift is an extremely aerial bird species (*6*) with short arm-wings and very long hand-wings. An adult swift has a streamlined body: a short, forked tail and long, curved scythe-like wings (Fig. 1). The average wing chord (the length of the cross section in the flight direction) along the hand-wing is approximately 5 cm.

Quantitative measurements of the flow patterns near a wing in flight are required to discover the lift-generating mechanisms. Such measurements on a real wing of a bird in flight are difficult and have not yet been done. Experiments quantifying the flow at some distance behind a flying bird have been carried out in a wind tunnel (*7*), but the resulting pictures of the disturbances in the air do not indicate exactly what happens at the wings.

Flow patterns in air and in water are the same as long as the flow is studied at the same Reynolds number (*Re*). *Re* expresses the relative importance of inertial over viscous forces in a dimensionless way: $Re = vl\,\nu^{-1}$, where v is the velocity in m s^{-1}, l is a relevant measure of length in m, and ν is the kinematic viscosity (the ratio of viscosity over density) in m^2 s^{-1}.

The *Re* number of a swift wing with an average chord length of 5 cm, gliding at an average speed of 11 m s^{-1} [the mean measured value for free-gliding swifts under conditions without wind (*8*)] in air of 20°C, at sea level, is 37,500.

We used a 1.5-times-enlarged and a real-size physical model of a swift wing in fast gliding posture (60° sweep of the hand-wing leading edge, based on direct observations and series of pictures of gliding swifts) to study the interactions with water in our recirculating water tunnel using DPIV (*4–6*).

Runs with the large model revealed the presence of a prominent LEV on top of the hand-wing. An angle of attack relative to the arm-wing chord as small as 5° with respect to the oncoming flow readily provided a stable LEV on top of the hand-wing. The wing was illuminated with a 3-cm-thick laser sheet perpendicular to the flow, in four planes successively. The results of the DPIV analysis of the pictures taken from behind are shown in Fig. 2. The LEV can be easily recognized in each vector field. The LEV core diameter increases from the wrist (Fig. 2A) toward the wing tip (Fig. 2C), indicating that the LEV has a conical shape. The vortex center is located above the wing and follows the wing inward of the leading edge toward the tip. Two cm behind the wing (Fig. 2D), the center is in a position inward from the wing tip, and the core diameter is still increasing. The maximum downwash flow velocity increases along the wing (with the LEV strength) and is twice as high at the wing tip (Fig. 2, C and D) compared with the position just behind the arm-wing (Fig. 2A), which indicates lift increase along the wing. The maximum downward velocity component at the wing tip is about 10% of the free-flow velocity.

The real-size cast of the swift wing showed the same flow patterns with stable LEVs at three speeds when tested at an angle of attack of about 10° relative to the proximal arm-wing chord. Figure 3A shows the increase of the LEV radius. The rotational velocities increase with the flow speed, but that does not substantially affect the radius of the vortex. Figure 3B shows how the distance between the leading edge of the wing and the vortex center increases to reach values of about 4 cm near the tip. This effect is also virtually independent of the flow velocity. These data are combined in the artist's impression of the total flow on the wings of a gliding swift in Fig. 4.

LEVs are robust, lift-producing aerodynamic flow systems allowing high angles of attack (*9*). At high angles of attack, the drag component of the aerodynamic force is large. We assume that swifts take advantage of the high lift as well as the high drag component of the LEVs to increase their agility in flight. They can, for example, use the high angle-of-attack LEVs to brake in midair without losing height immediately, as they do while catching insects in flight.

Conventional aerodynamic profiles provide high lift and low drag at high velocities under small angles of attack. The attached flow pattern is vulnerable because high angles of attack easily cause separation and uncontrolled stall.

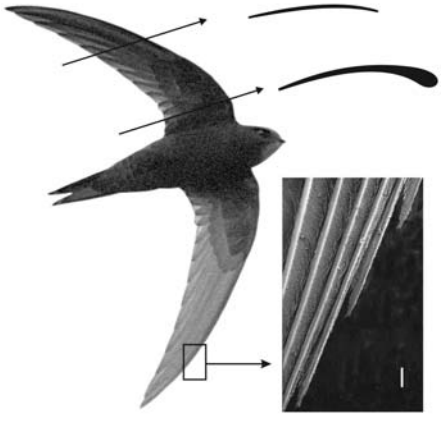

Fig. 1. Adult common swift (*Apus apus*) in gliding flight showing the torpedo-shaped body and the scythe-shaped wings with relatively short arm-wings and long slender hand-wings [picture: J. F. Cornuet]. Cross-sectional profiles through the arm-wing and the hand-wing taken from the indicated positions are shown. The inset is a scanning electron microscope picture of the sharp leading edge of the hand-wing (the white scale bar is 100 μm). The pointed barbs of the narrow anterior vane of the outermost primary feather form a serrated sharp cutting edge.

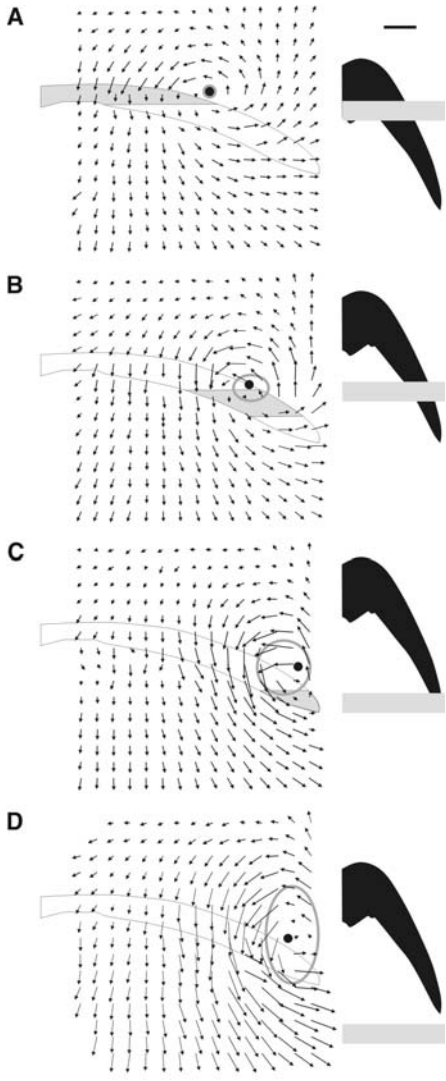

Fig. 2. Results of flow visualization from DPIV near a 1.5-times-enlarged model of a swift wing in a water tunnel. The *Re* number based on an average chord length of 7.5 cm is 37,500. Equally distributed flow vector maps are calculated from vertical particle displacements in four planes perpendicular to the flow, filmed from the rear at three positions on the hand-wing (**A**, **B**, and **C**) and at one position just behind the wing (**D**). The outline of the wing model is indicated in each case. A 3-cm-thick laser sheet was used for illumination of the particles. A gray area on the wing outlines in (A), (B), and (C) indicates the position of the laser sheet. The gray bar in each of the small pictures of the wing model in top view on the right gives an indication of the position and width of the laser sheet in top view. The scale bar (top right in A) is 5 cm and relates to all wing model drawings in top view. The flow in (D) shows the resulting rotation and the position of the vortex behind the wing (Movie S1); the position of the core is above the wing and slightly inward from the wing tip. The vectors are drawn at the same scale in all four panels. The LEV center is indicated with a black dot; the gray loops represent the core diameter at the level of maximum vorticity in each velocity diagram. Each loop approximates the solid-body rotation core radius.

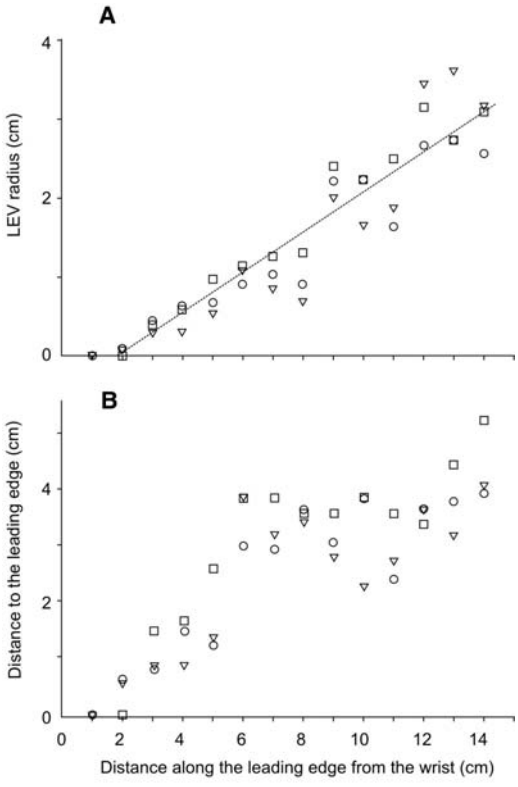

Fig. 3. Results of measurements in a water tunnel of LEV characteristics on a real-sized swift wing model at three speeds (*Re* numbers 3750, 7500, and 22,500) indicated by symbols: square, 0.05 m s^{-1}; circle, 0.1 m s^{-1}; triangle, 0.3 m s^{-1}. (**A**) The LEV radius from the wrist to the tip of the wing with the linear regression line through all data points (r^2 = 0.89). (**B**) The increase of the distance between the leading edge and the center of the vortex, measured perpendicular to the leading edge.

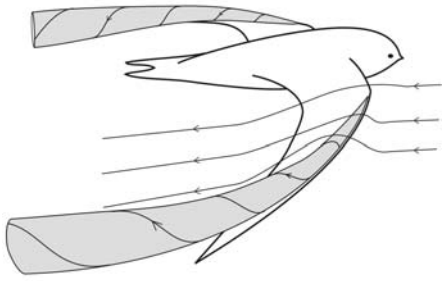

Fig. 4. Artist's impression of the conical LEVs on the wings of a swift in gliding flight. The oncoming flow is deflected downward by the attached LEV system, showing the lift-generating downwash. LEV separation starts at the wrists. From there the LEVs are attached over most of the wing length but start to go upward and inward approaching the wing tip and behind it.

Many birds use swept-back hand-wings during gliding. The sweep-back angle of pigeons, for example, varies in relation to gliding speed (*10*). Landing in most birds requires high lift and high drag at low speeds; LEVs on swept-back hand-wings kept at high angles of attack provide these forces and make landing on a branch possible. Birds use the high lift to keep the right altitude and use the high drag to brake during the approach glide.

Here, we have shown that LEVs do not require large angles of attack and can be generated at *Re* numbers as low as 3750. We speculate that LEVs are also present during flapping flight in the swift and in other birds. We propose, furthermore, that the arm-wing and hand-wing in birds play different roles. The arm-wing is typically built to use the conventional aerodynamic principle with attached flow, whereas the hand-wing can induce airflow separation, resulting in a LEV to generate lift. This changes the general view of how birds fly, and we think that the consistent difference in the anatomy between arm-wing and hand-wing in birds can now be better understood.

References and Notes

1. C. P. Ellington, C. van den Berg, A. P. Willmott, A. L. R. Thomas, *Nature* **384**, 626 (1996).
2. M. H. Dickinson, F. O. Lehmann, S. P. Sane, *Science* **284**, 1954 (1999).
3. R. B. Srygley, A. L. R. Thomas, *Nature* **420**, 660 (2002).
4. E. J. Stamhuis, J. J. Videler, *J. Exp. Biol.* **198**, 283 (1995).
5. E. J. Stamhuis, J. J. Videler, L. A. van Duren, U. K. Müller, *Exp. Fluids* **33**, 801 (2002).
6. Materials and methods are available as supporting material on *Science* Online.
7. G. R. Spedding, M. Rosén, A. Hedenström, *J. Exp. Biol.* **206**, 2313 (2003).
8. B. Bruderer, A. Boldt, *Ibis* **143**, 178 (2001).
9. M. V. Lowson, A. J. Riley, *J. Aircraft* **32**, 832 (1995).
10. C. J. Pennycuick, *J. Exp. Biol.* **49**, 509 (1968).
11. We thank J. F. Cornuet for permission to use the photograph of the gliding swift, J. Batsleer for collecting the data in Fig. 3, and N. Verloop (Dental Laboratory Vanderburg) for making the accurate cast of the swift wing. J. H. H. Videler, H. Videler, R. Gesser, and W. Wolff are acknowledged for critically reading the manuscript.

Supporting Online Material
www.sciencemag.org/cgi/content/full/306/5703/1960/DC1
Materials and Methods
References
Movie S1

31 August 2004; accepted 25 October 2004
10.1126/science.1104682